

SPATIALLY RESOLVED *STIS* SPECTRA OF BETELGEUSE'S UPPER CHROMOSPHERE AND CIRCUMSTELLAR DUST ENVELOPE

A. Lobel

Harvard-Smithsonian Center for Astrophysics, 60 Garden Street, Cambridge, 02138 MA, USA

ABSTRACT

The Hubble Space Telescope observed red supergiant Betelgeuse (α Ori) with the Space Telescope Imaging Spectrograph to investigate the outer atmosphere from spatially resolved spectra. We present a new set of seven high-resolution near-UV spectra observed with HST-*STIS* in fall 2002 and spring 2003, by scanning at chromospheric intensity peak-up position and six off-limb target positions up to three arcseconds away from the star. A small aperture is used to study and determine the thermal conditions and flow dynamics in the upper chromosphere and inner circumstellar dust envelope of this important nearby cool supergiant (M2 Iab).

We provide the first evidence for the presence of warm chromospheric plasma at least $3''$ away from Betelgeuse at $\sim 120 R_*$ ($1 R_* \simeq 700 R_\odot$) based on detailed spectroscopic observations of the Mg II h & k emission lines. Many other weak chromospheric emission lines as Fe II $\lambda 2716$, C II $\lambda 2327$, Al II] $\lambda 2669$, and Fe I $\lambda 2823$, are detected out to at least $1''$ in the spatially resolved *STIS* observations. The recent spectra reveal that α Ori's upper chromosphere extends far beyond the circumstellar H α envelope of $\sim 5 R_*$, determined from previous ground-based images. The changes of shape of the detailed Mg II line profiles observed in Betelgeuse's outer atmosphere are compared with detailed Mg II line profiles previously observed above the limb of the average quiet Sun. The profiles of the Mg II h & k , and the Si I resonance emission lines reveal a strong increase of asymmetry by scanning off-limb, signaling the outward acceleration of wind expansion in Betelgeuse's upper chromosphere beyond 200 mas ($\sim 8 R_*$).

We discuss detailed radiative transfer models that fit the *STIS* observations showing that the local kinetic gas temperature in the upper chromosphere exceeds 2600 K. Our radiation transport models for the IR silicate dust emission at $9.8 \mu\text{m}$ in the upper chromosphere show however that the ambient gas temperature remains below 600 K to sustain the presence of dust grains. Hence, the *STIS* spectra of Betelgeuse's upper chromosphere directly demonstrate that warm chromospheric plasma must co-exist with cool dusty plasma in its outer atmosphere.

Key words: Stars: α Orionis – chromospheres – dust – winds – mass-loss – spectroscopy – radiative transport

1. INTRODUCTION

Ongoing research of Betelgeuse's (HD 39801) extended chromosphere and dust envelope has recently provided important advances in understanding the dynamics and thermal structure of the atmospheres and winds of evolved stars. Detailed investigations of cool star atmospheres are much more intricate compared to hot stars because of enhanced atomic and molecular opacities and complicated dynamic activity (pulsation and convection), although late-type stars are one of the most important laboratories for stellar atmospheric physics. High-resolution spectroscopy of luminous cool stars provides fundamental information about the complex physical mechanisms that cause their exceptionally large mass-loss rates ($\dot{M} \geq 10^{-6} M_\odot \text{ yr}^{-1}$) by which these massive stars continuously replenish the interstellar medium with material that has been processed through nuclear fusion reactions, and from which many structures in circumstellar and interstellar environments originate. Unlike the supersonic accelerating winds of hot supergiants, the mass-loss mechanisms that drive the slower winds of cool supergiants like Betelgeuse are presently not well understood due to a persistent lack of high-quality ultraviolet spectra that probe the important physical properties of atmospheric regions located between the photosphere and the extended circumstellar dust envelope.

Spatially resolved raster scans observed with *STIS* using a small aperture across Betelgeuse's UV disk in HST Cycles 7 & 8 reveal subsonic oscillations of the inner chromosphere from radiative transfer fits to the detailed asymmetric profiles of the Si I $\lambda 2516$ resonance emission line (Lobel 2001, Lobel & Dupree 2001). The near-UV spectra show long-term changes of gas movements in the lower chromosphere with pulsations of the deeper -presently unresolved- stellar photosphere. For the first time, these two-dimensional *STIS* spectra provided direct evidence that α Ori's inner chromosphere oscillates non-radially, thereby occasionally exhibiting simultaneous up- and down-flows.

2. HST-STIS OBSERVATIONS OF 2002-2003

Recent *STIS* spectra of Betelgeuse have been observed in the fall of 2002 and spring of 2003 for GO 9369 in HST

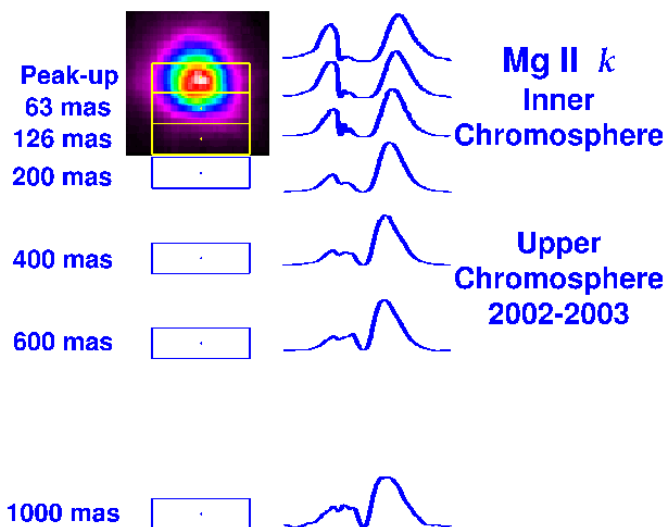


Figure 1. Spatially resolved STIS observations of the Mg II k resonance emission line across α Ori’s inner and upper chromosphere using the 63 by 200 mas aperture with respect to a false color near-UV image of the inner chromosphere. The Mg II line is scaled to the same intensity to show important profile shape changes.

Cycle 11; *A direct Test for Dust-driven Wind Physics*. The program investigates the detailed acceleration mechanisms of wind outflow in the outer atmosphere, the upper chromosphere and inner circumstellar dust envelope (CDE), of the nearby red supergiant. Using the exceptional capabilities of the STIS we observe the near-UV spectrum with $\lambda/\Delta\lambda \approx 33,000$ between 2275 Å and 3180 Å with spatially resolved raster scans across the chromosphere at 0, 200, 400, 600, & 1000 milli-arcseconds (mas) (Visit 1), at 0 & 2000 mas (Visit 2), and at 0 & 3000 mas (Visit 3). The spectra are observed with a small aperture of 63 by 200 mas, using exposure times ranging from 500 s at 200 mas to 8700 s at 3000 mas, yielding good $S/N \geq 20$. The spectra have been calibrated with CALSTIS v2.12 using the most recently updated calibration reference files. Wavelength calibration accuracies are typically better than ~ 1 detector pixel, or 1.3 km s^{-1} .

In previous work we modeled the detailed shape of the Mg II h & k resonance emission lines (Lobel & Dupree 2000). The lines have previously been observed (April 1998) by scanning across the inner chromosphere at 0, 63, and 126 mas, also using a slit size of 63×200 mas (Table 1). Figure 1 shows the Mg II k line profile at the respective slit positions up to 1000 mas, compared to an image of the near-UV continuum (in false colors) observed with HST-FOC (Lobel 2003a). The FWHM of the image is about twice the optical diameter of the supergiant of 56 mas. The central (self-) absorption core results from scattering opacity in the chromosphere. The asymmetry of the emis-

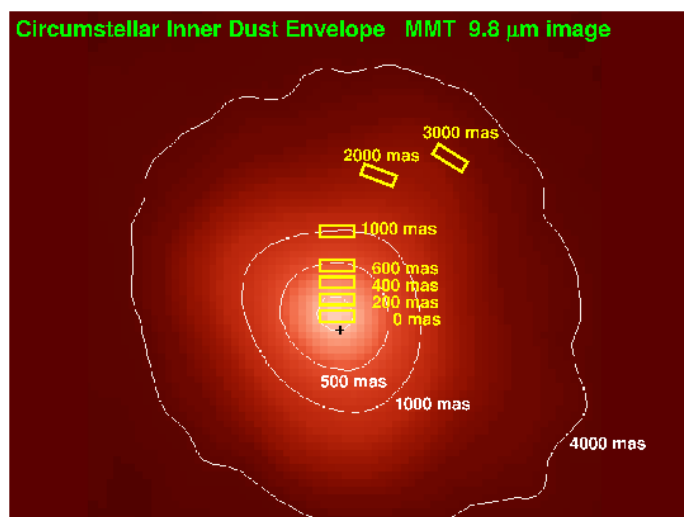


Figure 2. Relative aperture positions of spatially resolved spectroscopic observations with STIS in 2002-2003 with respect to a $9.8 \mu\text{m}$ image of α Ori’s inner circumstellar dust envelope from MMT-MIRAC2 (image adapted from Hinz et al. 1998).

sion line component intensities probes the chromospheric flow dynamics in our line of sight. The profiles observed in the upper chromosphere reveal an increase of asymmetry with a weaker short-wavelength emission component. It signals substantial wind outflow opacity in the upper chromosphere, which fastly accelerates beyond 200 mas ($\approx 8.1 R_*$). Figure 2 shows an image of Betelgeuse’s CDE observed with MMT-MIRAC2 in infrared light around $10 \mu\text{m}$. The outer intensity contour is drawn at $\sim 1\%$ of the non-interfered stellar peak intensity (~ 4000 mas) from the star’s position (*at cross*) in this interferometrically nulled image (Hinz et al. 1998). The relative target positions (TP) of the STIS aperture across the inner CDE are indicated.

3. WIND ACCELERATION IN THE UPPER CHROMOSPHERE

Figure 3 shows the detailed line profiles of the broad Mg II h & k emission lines formed in the inner and upper chromosphere of Betelgeuse. The resonance emission lines are observed up to $3''$ away from the supergiant photosphere, corresponding to $\sim 120 R_*$. The upper panel of Fig. 4 compares the Mg II k line profiles across the inner and upper chromosphere in velocity scale. The line fluxes are scaled to the maximum flux of the long-wavelength emission component. We observe a strong decrease of the short-wavelength emission component compared to the long-wavelength component by scanning outwards (toward larger TPs), which we also observe in resonance lines of Si I $\lambda 2516$ and $\lambda 2507$, and in Mg I $\lambda 2852$. The short-wavelength emission component of the Mg II k line is however blended with a weak Fe I line and a chromospheric Mn I line that can

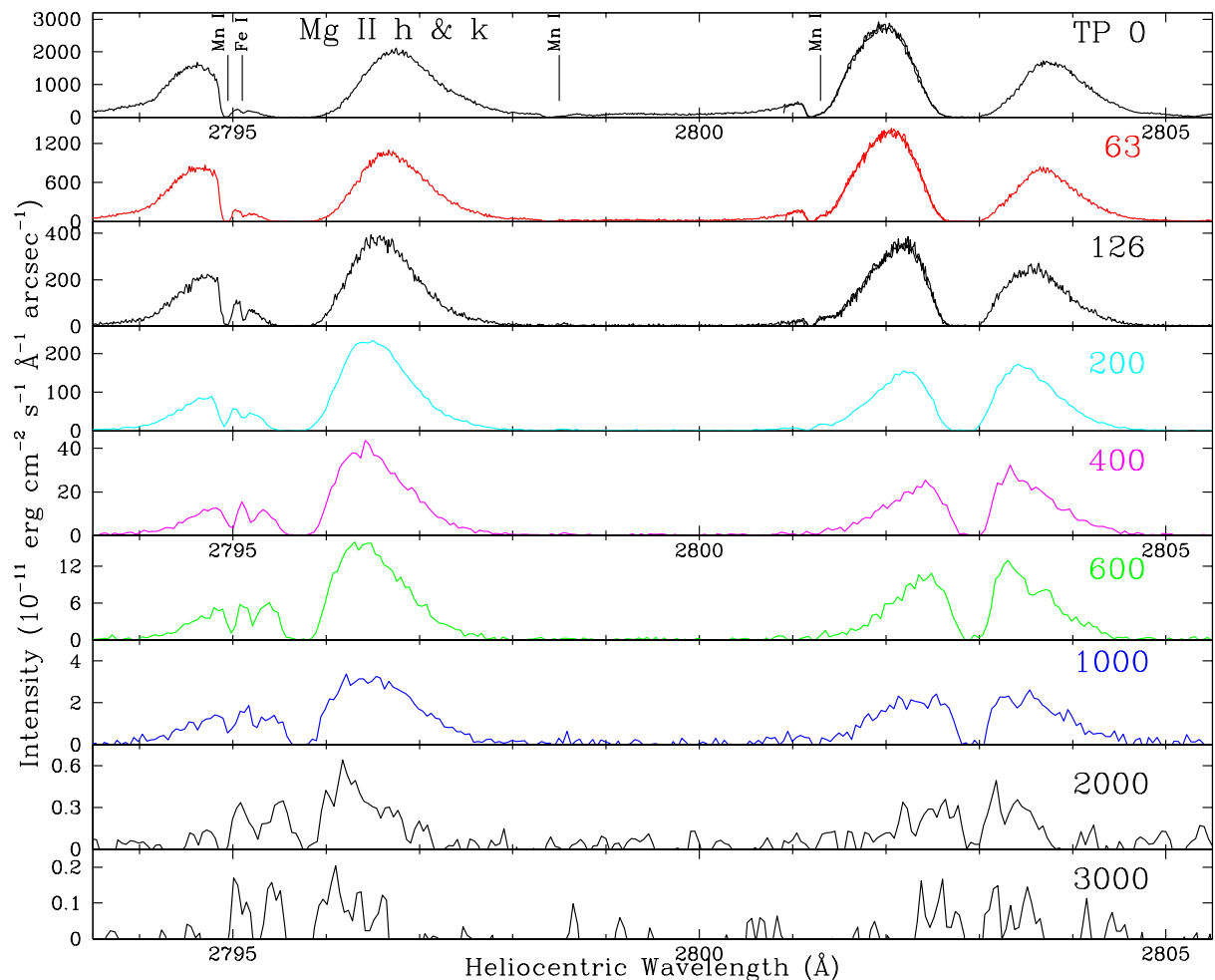


Figure 3. Spatially resolved STIS spectra of Mg II h & k emission lines from HST Cycles 7 & 11, observed off-limb in the chromosphere and circumstellar dust envelope of Betelgeuse with the 0.2×0.06 aperture out to 3 arcseconds.

Table 1. Spatially resolved spectroscopic exposures of α Ori observed with STIS during HST Cycle 7 (GO 7347), using high resolution grating E230H and the 0.2×0.06 aperture. Other STIS observations of Jan., Apr., & Sep. 1998, and March 1999 using the 0.1×0.03 aperture are not listed.

Obs. date	Dataset (MAST No.)	POS TARG (arcsec)	Total exp. time (s)	Science exp. (amount)	Aperture (name)
Apr. 1 1998	O4DE05090	-0.126, 0.0	460	1	0.2×0.06
	O4DE050A0	-0.063, 0.0	360	1	0.2×0.06
	O4DE050B0	0.000, 0.0	260	1	0.2×0.06
	O4DE050C0	0.063, 0.0	360	1	0.2×0.06
	O4DE050D0	0.126, 0.0	450	1	0.2×0.06

influence the k line asymmetry observed across the inner chromosphere. The lower panel of Fig. 4 shows four spatially resolved (scaled) Mg II k profiles from balloon observations (RASOLBA; Staath & Lemaire 1995) out to $9''$ above the limb of the average quiet Sun. Similar to Betelgeuse, the FWHM of the Mg II k (and h) line, and the width of the central self-absorption core, decreases with larger distances above the solar limb. These changes result from the decrease of electron density and microtur-

bulence velocity higher in the upper chromosphere, which decreases the scattering of photons along the line of sight. The central absorption cores of the Mg II lines in Betelgeuse ($d \sim 132$ pc) can also have narrow contributions from the Local Interstellar Medium (LISM), but which remain smaller ($\text{FWHM} \leq 25 \text{ km s}^{-1}$) than the width of the central absorption cores we observe at 2000 and 3000 mas (Lobel 2003b).

Table 2. Spatially resolved spectroscopic exposures of α Ori observed with STIS during HST Cycle 11 (GO 9369), using medium resolution grating E230M with the 0.2×0.06 and 0.1×0.03 apertures.

Obs. date	Dataset (MAST No.)	POS TARG (arcsec)	Total exp. time (s)	Science exp. (amount)	Aperture (name)
Oct. 14 2002	O6LX01020	0.000, 0.0	283	1	0.1×0.03
	O6LX01030	0.200, 0.0	600	1	0.2×0.06
	O6LX01040	0.400, 0.0	1000	1	0.2×0.06
	O6LX01050	0.600, 0.0	1849	1	0.2×0.06
	O6LX01060	1.000, 0.0	1400	1	0.2×0.06
Mar. 02 2003	O6LX01070	1.000, 0.0	5800	2	0.2×0.06
	O6LX02060	0.000, 0.0	300	1	0.1×0.03
Apr. 23 2003	O6LX02070	2.000, 0.0	8663	3	0.2×0.06
	O6LX03060	0.000, 0.0	300	1	0.1×0.03
	O6LX03070	3.000, 0.0	8663	3	0.2×0.06

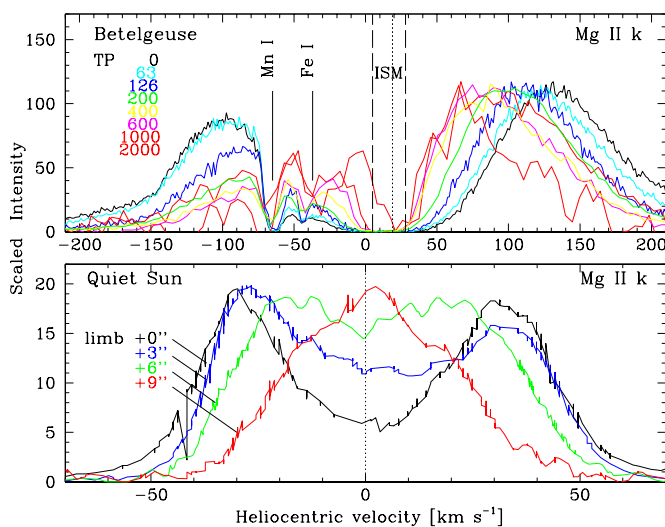


Figure 4. Spatially resolved STIS spectra of the Mg II k emission line observed across the inner and upper chromosphere of Betelgeuse (upper panel), compared to spatially resolved spectra of the k line from balloon observations (lower panel) above the limb of the average quiet Sun (see text).

4. Si I $\lambda 2516$ LINE PROFILE CHANGES

In previous work we modeled the detailed shape of the unblended Si I $\lambda 2516$ resonance emission line (Lobel & Dupree 2001). The line was observed by scanning across the inner chromosphere at 0, 25, 50, and 75 mas, using an aperture size of 30×100 mas. Figure 5 shows double-peaked Si I line profiles observed across the inner chromosphere in March 1999. The central (self-) absorption core results from scattering opacity in the inner chromosphere. The asymmetry of the emission component intensities probes the chromospheric flow dynamics in our line of sight. The line profiles of the outer chromosphere beyond 75 mas are observed with a slit size of 63×200 mas (Table 2). The profiles appear red-shifted and reveal weaker

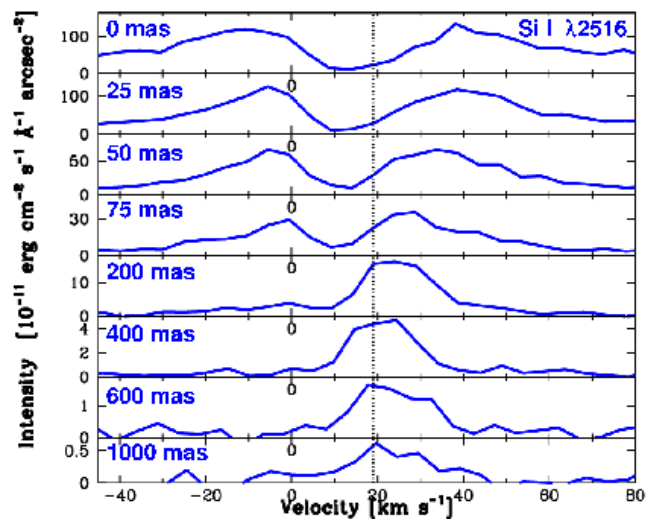


Figure 5. The detailed shape of the unblended Si I $\lambda 2516$ emission line reveals a strong increase of profile asymmetry by scanning from the inner to the outer extended chromosphere of α Ori. The violet emission wing of the line strongly decreases beyond 200 mas due to increased blueshifted scattering opacity in an expanding upper chromospheric wind.

short-wavelength emission components by scanning outwards. It signals substantial wind outflow opacity in the upper chromosphere, which fastly accelerates beyond 200 mas. The shape of these unsaturated Si I emission lines is very opacity sensitive to the local chromospheric velocity field in the line formation region. Similar as for the Mg II lines, the outward decrease of intensity of the short-wavelength emission component signals fast acceleration of wind outflow in the upper chromosphere. Previous detailed radiative transfer modeling of Si I $\lambda 2516$ revealed that α Ori's inner chromosphere oscillates non-radially in September 1998 (see Sect. 6).

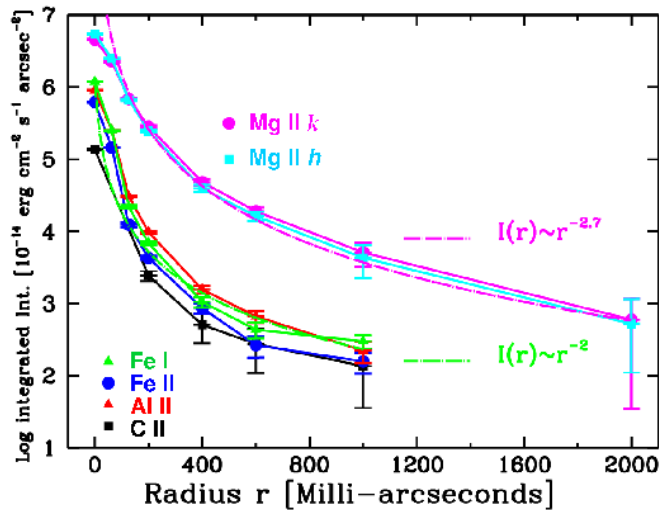


Figure 6. Integrated intensities of the Mg II resonance emission lines observed in spatially resolved *STIS* spectra of Betelgeuse’s upper atmosphere. A best fit to the radial intensity distributions is obtained for $I(r) \sim r^{-2.7}$, signaling important radiative transfer effects on the detailed line profile formation (see Fig. 3). The flux in the Mg II emission lines decreases by a factor of 10^4 compared to the flux at chromospheric disk center.

5. RADIAL INTENSITY OF CHROMOSPHERIC LINES

We observe various ion emission lines as Fe II $\lambda 2716$ (UV 62), Al II $\lambda 2669$ (UV 1), and C II $\lambda 2327$ (UV 1) out to $1''$ in the upper chromosphere (see Fig. 3 of Lobel et al. 2003c). We select unblended single-peaked emission lines without a central self-absorption core to determine the radial intensity distribution $I(r)$ across the chromosphere from wavelength integration beyond the line wings. Figure 6 compares the $I(r)$ of the three ion lines and of Fe I $\lambda 2823$ (UV 44) with the intensity distribution observed for the Mg II h & k lines. The lines of the inner chromosphere were observed in April 1998 with $R \sim 114,000$ at 0, 63, and 126 mas, while the lines in the upper chromosphere ($r \geq 200$ mas) have been observed with medium resolution in fall 2002. The spatial scans are however observed with the same slit size of 63×200 mas, so that integrated line intensities can be compared. The intensity errorbars are computed from the *STIS* pipeline flux calibration errors, while the radius errorbars are derived from the projected slitwidth. We observe that the $I(r)$ of single-peaked neutral and ion emission lines are very similar across the chromosphere. The lines become rather optically thin in the upper chromosphere with a density dependent $I(r)$ that is best fit with $I(r) \simeq \text{const} \times r^{-2}$. In general the single-peaked neutral emission lines can be observed somewhat farther into the upper chromosphere with larger S/N compared to the ion lines, although their $I(r)$ do not differ significantly within the errors. The $I(r)$

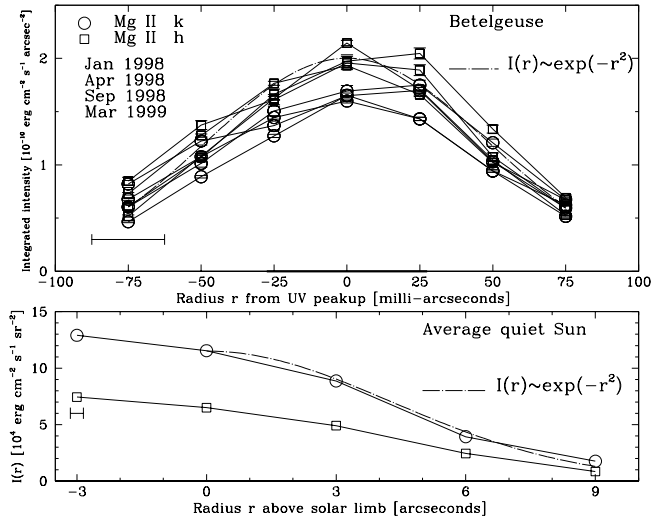


Figure 7. A comparison of integrated line intensities of Mg II h & k derived from spatially resolved observations across the inner chromosphere of Betelgeuse (upper panel) and the limb of the Sun (lower panel). The off-limb radial intensity distributions follow an exponential dependence, despite the large difference in chromospheric extension for Betelgeuse and the Sun.

distribution for the optically thick and self-absorbed Mg II lines differs however significantly with $I(r) \simeq \text{const} \times r^{-2.7}$. The steeper intensity distribution (note the logarithmic scale for I) signals important radiative transfer effects for the formation of the detailed Mg II line profiles.

The upper panel of Fig. 7 shows the $I(r)$ -distribution for the Mg II lines in four spatially resolved *STIS* observations during 1998-99. The raster scans have been observed with the smallest aperture of 30×100 mas across the inner chromosphere of Betelgeuse out to $r = \pm 75$ mas. The average $I(r)$ is best fits with an exponential distribution of $I(r) \sim \exp(-r^2)$ (dash-dotted line). In the lower panel of Fig. 7 we wavelength integrate the Mg II line intensities observed above the limb of the average quiet Sun (lower panel of Fig. 4). We also obtain a best fit for an exponential radial intensity dependence of these optically thick resonance emission lines above the solar limb. Since it has been suggested that the solar magnesium chromosphere can be sustained by the dissipation of mechanical waves, the *STIS* observations of Betelgeuse can provide new indications that similar heating mechanisms are viable for heating its inner chromosphere. Conversely, the tremendously large difference observed for the chromospheric extension of the Sun (0.01 to $0.02 \times R_{\odot}$) compared to Betelgeuse ($\sim 120 \times R_{*}$), signals that the efficiency of these chromospheric heating mechanisms is very different and strongly determined by the outward acceleration mechanism(s) in the (magnetic) upper photosphere of a yellow dwarf star compared to the very extended (presumably non-magnetic) atmosphere of a red supergiant star.

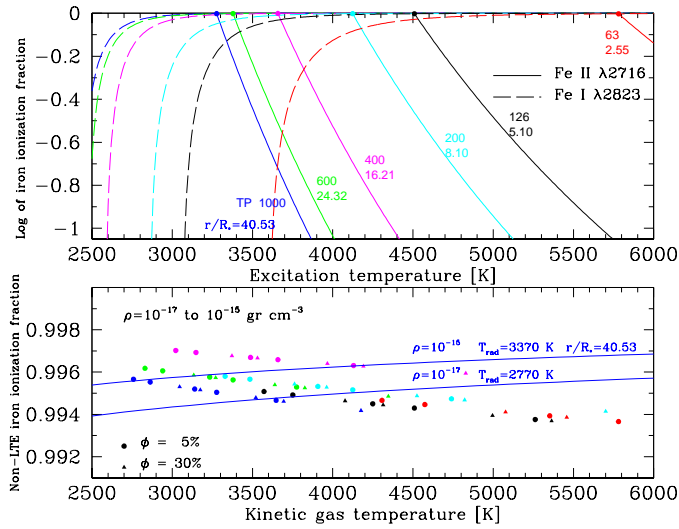


Figure 8. Iron ionization fractions computed from Fe I and Fe II emission line intensities observed out to $1''$ in the chromosphere of α Ori (dots in upper panel). The corresponding non-LTE ionization fractions are computed (lower panel) for 5 gas density values (filled dots and triangles) with a diluted radiation field of 3000 K, yielding gas kinetic temperatures above 2600 K. Colors in upper and lower panels correspond (see text).

6. SEMI-EMPIRIC MODEL FOR THE CHROMOSPHERE

In the upper panel of Fig. 8 we compute the iron ionization fraction from the radial intensity distribution of the single-peaked Fe I $\lambda 2823$ (dashed lines) and Fe II $\lambda 2716$ (solid line) emission lines. The intersection of the ionisation curves (solid dots) provides the excitation temperature corresponding to the observed line intensity ratios for spontaneous emission in these (optically thin) line transitions for TPs up to 1000 mas. We assume the iron solar abundance in our computations. The lower panel in Fig. 8 shows these iron non-LTE ionization fractions between 99.3% and 99.7%, which correspond to kinetic gas temperatures between 2600 K and 5800 K, we compute for five local gas densities ρ for warm chromospheric plasma between 10^{-17} and 10^{-15} gr cm^{-3} (filled colored symbols correspond to line colors in the upper panel). This gas temperature range corresponds to partial non-LTE iron ionization due to a diluted radiation field of $T_{\text{rad}} \approx 3000$ K (e.g. full drawn lines are computed for TP 1000 where $r/R_* = 40.53$), typical for the upper chromosphere of Betelgeuse. The graphs are computed with volume filling factors ϕ for warm chromospheric plasma of 5% (dots) and 30% (triangles). We compute that hydrogen is almost neutral for these conditions in the upper chromosphere.

We compute that the warm chromospheric plasma assumes kinetic gas temperatures above 2600 K out to $1''$ for a range of realistic gas density values we determine in the next Section from detailed radiative transport models of

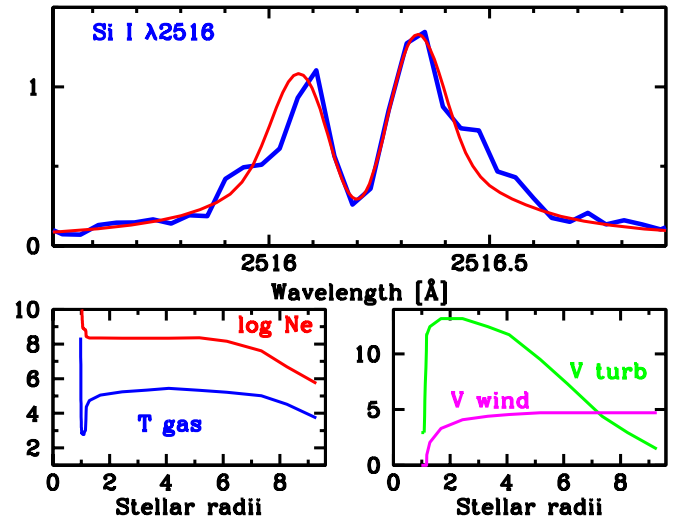


Figure 9. Detailed non-LTE radiative transfer fits (red line in upper panel) to the spatially resolved Si I $\lambda 2516$ emission line observed at 75 mas (blue line). The corresponding thermal and dynamic structures of the inner chromosphere model (lower panels) are varied in movie sequences to illustrate the goodness of fit. T_{gas} is shown in kK units, and V_{wind} and V_{turb} in km s^{-1} units.

the inner CDE. These chromospheric gas densities correspond to the range of model electron densities N_e required to compute the self-absorbed shape of the Si I $\lambda 2516$ resonance line in Fig. 9. The best fit (solid red line in upper panel) to the spatially resolved line profile observed at 75 mas (solid blue line) is obtained for a thermal model of the inner chromosphere ($r \leq 10 R_*$) (lower left panel) with $T_{\text{gas}} \leq 5500$ K (where $N_e \approx 2.8 \cdot 10^8 \text{ cm}^{-3}$) and N_e decreases outward. The dynamic model (lower panel right) requires projected microturbulence velocities with a local maximum of $\sim 13 \text{ km s}^{-1}$, and an outward accelerating (gas) wind velocity increasing to 4.5 km s^{-1} , to match the asymmetric shape and width of the Si I emission line. A more extensive discussion on the determination of the semi-empiric model for the inner chromosphere of Betelgeuse with detailed radiative transfer fits is provided in Lobel & Dupree (2001). Comprehensive animations demonstrating important radiative transfer effects on the formation of the detailed Si I line profile by varying the $\log(N_e)$, V_{turb} , and V_{wind} chromospheric model structures are available with this paper, at cfa-www.harvard.edu/~alobel, and in the Cool Stars 13 Conference website at www.hs.uni-hamburg.de/cs13/day5/04_Lobel.ppt

7. SEMI-EMPIRIC MODEL OF INNER DUST ENVELOPE

We determine the model parameters of Betelgeuse's inner CDE with radiative transfer in spherical geometry using the DUSTY code (Ivezić & Elitzur 1995; Lobel et al. 1999). Figure 10 shows the best fit to the weak silicate dust

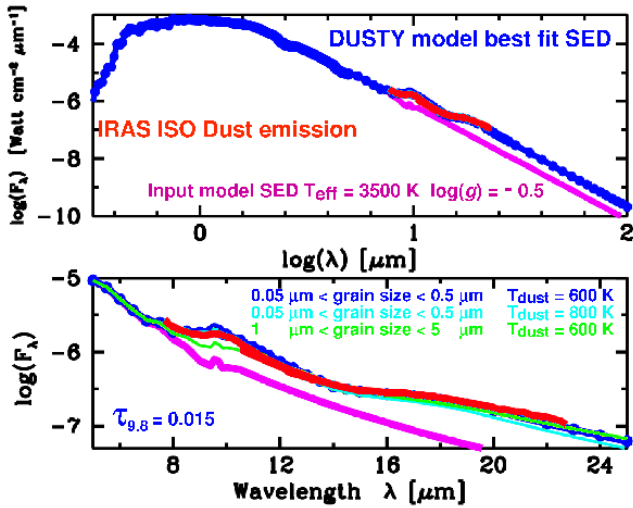


Figure 10. Best fit with DUSTY (dotted line in upper panel) to the IRAS 9.8 μm silicate dust emission of α Ori (red line). The detailed stellar input spectrum (magenta line) is processed through the model of the circumstellar dust envelope (see Fig. 12). The best fit is obtained for olivine grain composition (blue line in lower panel) (see text).

emission feature observed at 9.8 μm with *IRAS* (or *ISO*) (red solid lines). The detailed (Kurucz) photospheric input model with $T_{\text{eff}}=3500$ K and $\log(g)=-0.5$ is processed through a model of the CDE (Lobel et al. 2000). The best fit yields an inner dust condensation radius $R_c \simeq 573$ mas ($\sim 23.2 R_*$), where $\rho_{\text{gas}} \sim 5 \cdot 10^{-16}$ gr cm^{-3} for the cool ambient gas component. We assume the canonical value of 200 for the gas-to-dust density ratio, although an order of magnitude larger can still be adopted for this cool supergiant star. The best model fit yields a silicate dust condensation temperature of $T_{\text{dust}} \leq 600$ K (blue solid dotted lines), composed of olivine grains with a size distribution $n(a) \sim a^{-3.5}$, and $0.05 \mu\text{m} \leq a \leq 0.5 \mu\text{m}$. We compute that the 9.8 μm flux optical depth of α Ori’s inner CDE is small with $\tau_{9.8}=0.015$. Figure 11 shows the corresponding best model fit (green line) to the dust surface brightness of the inner CDE observed in the 10 μm MMT images out to 4". The relative dust emission intensities computed with the model in front of the inner dust cavity (vertical dashed line) are not shown. Danchi et al. (1994) find from visibility curves very little dust radiation coming from distances below 950 mas, while Sutton et al. (1977) observe that less than 20 % of the excess radiation at 10 μm is emitted by dust between 6 R_* and 12 R_* from α Ori.

The upper panel of Fig. 12 shows the kinetic gas temperature structure of the warm chromospheric plasma computed with $\rho_{\text{gas}}=5 \cdot 10^{-16}$ gr cm^{-1} for $\phi=1\%$ and 100% (bold red lines). The model for the inner chromosphere is computed with detailed radiative transfer fits to $\text{H}\alpha$ and Mg II (Lobel & Dupree 2000). We compute that the temperatures of the upper chromospheric plasma do not de-

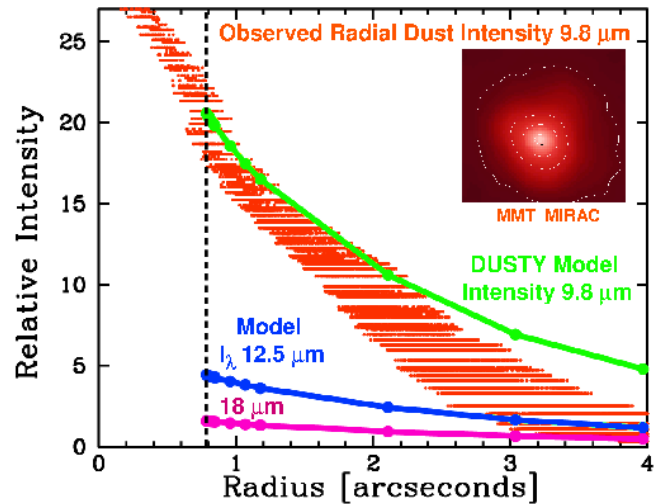


Figure 11. Best fit with DUSTY to the observed 9.8 μm radial intensity distribution of α Ori’s inner dust envelope from MMT-MIRAC2 images. Model I_λ ’s at 12.5 and 18 μm are also shown.

crease to below 2600 K in Sect. 6. The lower panel of Fig. 12 shows the model of the CDE we compute from the best fit to the silicate dust emission observed in the upper chromosphere. To condense dust grains out of the gas phase the ambient gas temperature remains below the dust temperature $T_{\text{dust}} \leq 600$ K (magenta line). Hence warm chromospheric plasma must co-exist with cool gas of $T_{\text{gas}} \leq 600$ K beyond 600 mas (Lobel et al. 2004). Radiation pressure onto dust accelerates the grains to a terminal (dust) outflow velocity of $\sim 13 \text{ km s}^{-1}$ (green line). The dust-gas interaction causes the wind acceleration by dust-gas drag forces. The acceleration of the warm wind is observed with *HST-STIS* in the upper chromosphere of Betelgeuse from the increase of emission line asymmetry (Sect. 4).

8. CONCLUSIONS

- Based on the $\text{Mg II } h \text{ \& } k$ emission lines we provide the first evidence for the presence of warm chromospheric plasma up to three arcseconds away from the star at $\sim 120 R_*$ ($1 R_* \simeq 700 R_\odot$). Other strong emission lines of $\text{Fe II } \lambda 2716$, $\text{C II } \lambda 2327$, and $\text{Al II }] \lambda 2669$ are significantly detected out to a full arcsecond. The *STIS* spectra reveal that Betelgeuse’s upper chromosphere extends far beyond the circumstellar $\text{H}\alpha$ envelope of $\sim 5 R_*$, determined from previous ground-based imaging (Hebden et al. 1987).
- The flux in the broad and self-absorbed resonance lines of Mg II decreases by a factor of 10^4 compared to the flux at chromospheric disk center. We observe strong asymmetry changes in the $\text{Mg II } h \text{ \& } k$, $\text{Si I } \lambda 2516$, and $\lambda 2507$ resonance emission line profiles when scanning off-limb, signaling outward acceleration of gas outflow

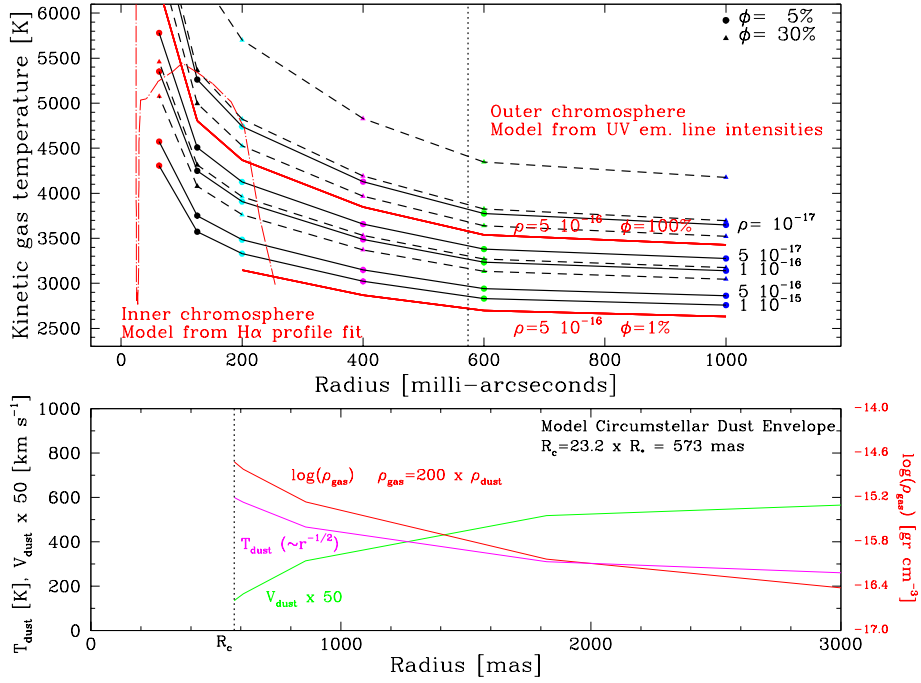


Figure 12. Kinetic gas temperatures computed for the upper chromosphere of Betelgeuse with 5 gas density values $10^{-17} \leq \rho \leq 10^{-15}$ gr cm^{-3} and volume filling factors for chromospheric plasma ϕ of 5% (dots in upper panel) and 30% (triangles). Upper chromospheric T_{gas} -values with $\phi=1\%$ and 100% for $\rho = 5 \cdot 10^{-16}$ gr cm^{-3} (bold red lines) remain above 2600 K. Best fits to dust emission in the upper chromosphere require model temperatures (magenta line in lower panel) of ambient gas below 600 K to sustain the presence of silicate dust (see text).

in the upper chromosphere. It directly demonstrates that the warm chromospheric wind of Betelgeuse extends far beyond the dust condensation radius determined from stationary dust-driven wind acceleration models.

- A detailed comparison of profile changes observed for the Mg II h & k lines with HST-*STIS* across the chromosphere of Betelgeuse reveals a striking resemblance to the emission line profile changes observed across the limb of the average quiet Sun. We observe that the integrated radial intensities $I(r)$ of the Mg II lines follow an exponential distribution ($I(r) \sim \exp(-r^2)$) for the magnesium chromosphere of the Sun and for the inner chromosphere of Betelgeuse out to a distance r of ~ 75 mas. On the other hand, our measurements reveal that the integrated line intensities with distance in the *upper* chromosphere beyond 75 mas cannot be modeled with an exponential distribution, and require a sharply peaked function of $I(r) \sim r^{-2.7}$.
- We compute that the local kinetic gas temperatures of the warm chromospheric gas component in the outer atmosphere exceed 2600 K, when assuming local gas densities of the cool gas component we determine from radiative transfer models that fit the $9.8 \mu\text{m}$ silicate dust emission and its radial surface brightness. The spatially resolved *STIS* spectra directly demonstrate that warm chromospheric plasma co-exists with cool

gas in Betelgeuse’s circumstellar dust envelope. The recent *STIS* data can therefore support the dust-gas interaction driving mechanism, yielding the high mass-loss rates observed in cool supergiants and AGB stars. From a thermodynamic point of view however, the uniform dusty wind model fails to account for the large local kinetic gas temperature differences because the warm chromospheric gas ($T_{\text{gas}} \geq 2600$ K) is observed far inside the CDE ($T_{\text{dust}} \leq 600$ K), out to $3''$, $\sim 120 R_*$ away from Betelgeuse.

ACKNOWLEDGEMENTS

This research is based on data obtained with the NASA/ESA Hubble Space Telescope, collected at the STScI, operated by AURA Inc., under contract NAS5-26555. Financial support has been provided by STScI grant HST-GO-09369.01.

REFERENCES

- Danchi, W. C., Bester, M., Degiacomi, C. G., Greenhill, L. J., & Townes, C. H. 1994, *AJ*, 107, 1469
- Hebden, J. C., Eckart, A., & Hege, E. K. 1987, *ApJ*, 314, 690
- Hinz, P.M., Angel, J.R.P., Hoffmann, W.F., McCarthy, D.W., Jr., et al. 1998, *Nature*, 395, 251
- Ivezic, Z., & Elitzur, M. 1997, *ApJ*, 445, 415
- Lobel, A. 2001, *ASP Conf. Proc.*, 242, 241, San Francisco
- Lobel, A. 2003a, *The Future of Cool-Star Astrophysics*, Proc. 12th Cambridge Workshop on Cool Stars 2001, Stellar Systems, & The Sun, 329, Online publication Univ. Colorado

- Lobel, A. 2003b, BAAS, 203, 4305, (poster at cfa-www.harvard.edu/~alobel)
- Lobel, A., Aufdenberg, J., Dupree, A. K., Kurucz, R. L., Stefanik, R. P., & Torres, G. 2003c, Stars as Suns: Activity, Evolution and Planets, Proc. IAU, Symp. No. 219, 158, Sydney, Australia
- Lobel, A., Aufdenberg, J., Dupree, A. K., Kurucz, R. L., Stefanik, R. P., & Torres, G. 2004, CfA Press Release, No. 04-03, Online at cfa-www.harvard.edu/press/pr0403.html
- Lobel A., Bagnulo S., Doyle J. G., & Power C., 2000, MNRAS, 317, 391
- Lobel, A., Doyle J. G., & Bagnulo S., 1999, A&A, 343, 466
- Lobel, A., & Dupree, A. K. 2001, ApJ, 558, 815
- Lobel, A., & Dupree, A. K. 2000, ApJ, 545, 454
- Staaath, E., & Lemaire, P. 1995, A&A, 295, 517
- Sutton, E. C., Storey, J. W. V., Betz, A. L., Townes, C. H., & Spears, D. L. 1977, 217, L97